Journal of
Materials Chemistry A

Accepted Manuscript

This article can be cited before page numbers have been issued, to do this please use: S. Liu, K.S. Hui, K. N. Hui, H. Li, K. W. Ng, J. Xu, Z. Tang and S. C. Jun, *J. Mater. Chem. A*, 2017, DOI: 10.1039/C7TA05493A.

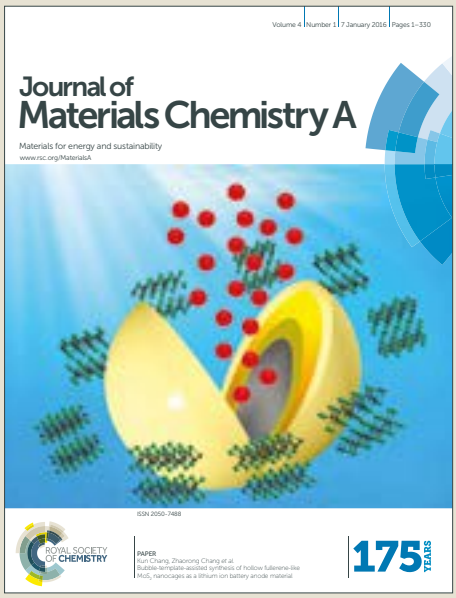

ROYAL SOCIETY OF CHEMISTRY

rsc.li/materials-a

DOI: 10.1039/C7TA05493A

Journal of Materials Chemistry A

ARTICLE

Asymmetric Supercapacitor with Excellent Cycling Performance Realized by Hierarchical Porous $NiGa_2O_4$ Nanosheets

Shude Liu[a], Kwan San Hui[b,*], Kwun Nam Hui[c,*], Hai-Feng Li[c], Kar Wei Ng[c], Jincheng Xu[c], Zikang Tang[c], and Seong Chan Jun[a,*]

Received 00th January 20xx,
Accepted 00th January 20xx

DOI: 10.1039/x0xx00000x
www.rsc.org/

Rational design of composition and electrochemically favorable structure configuration of electrode materials are highly required to develop high-performance supercapacitors. Here, we report our findings on the design of interconnected $NiGa_2O_4$ nanosheets as advanced cathode electrodes for supercapacitors. Rietveld refinement analysis demonstrates that the incorporation of Ga in NiO leads to a larger cubic lattice parameter that promotes faster charge-transfer kinetics, enabling significantly improved electrochemical performance. The $NiGa_2O_4$ electrode delivers a specific capacitance of 1508 F g^{-1} at a current density of 1 A g^{-1} with the capacitance retention of 63.7% at 20 A g^{-1}, together with excellent cycling stability after 10000 charge–discharge cycles (capacitance retention of 102.4%). An asymmetric supercapacitor device was assembled by using $NiGa_2O_4$ and Fe_2O_3 as cathode and anode electrodes, respectively. The ASC delivers a high energy density of 45.2 Wh kg^{-1} at a power density of 1600 W kg^{-1} with exceptional cycling stability (94.3% cell capacitance retention after 10000 cycles). These results suggest that $NiGa_2O_4$ can serve as a new class cathode material for advanced electrochemical energy storage applications.

1. Introduction

The ever-growing demands for high-power and high-energy storage applications, such as portable electronic devices and hybrid electric vehicles, have stimulated the urgent development of supercapacitors with high energy density, high power density, and long cycle life. Intensive research efforts have been undertaken to develop nanostructured electrode materials to improve electrochemical performance.[1-3] Transition metal oxides, which exhibit fast surface Faradaic redox reactions, possess higher theoretical specific capacitances in comparison to carbonaceous materials featuring reversible ion electrosorption at the electrostatically charged electrode surface.[4, 5] Among these, Ni-based spinel materials with the general formula NiM_2O_4 (M = Co, Mn, and Fe) have been intensively studied as advanced cathode materials for supercapacitors, owing to their high theoretical specific capacitance, environmental friendliness, good chemical compatibility with nickel substrates, and rich redox reaction property.[6-10] Although energy densities have been greatly improved in spinel-type Ni-based supercapacitors, the rate capability and cycling stability accompanied by those supercapacitors are typically low, owing to low electronic conductivity and inferior mechanical/chemical stability.[11, 12] To date, incorporating suitable elements in pseudocapacitive electrode materials has been regarded as an effective approach to tailor the electrochemical performance of cathode electrode in the supercapacitors. Therefore, the development of new class spinel materials with desirable geometry should be explored. It came to our attention that $NiGa_2O_4$ spinel structure with Ga trivalent element has been widely studied in the areas of transparent conduction oxide,[10] optical absorption measurements,[13] and photocatalytic water splitting[14-17] owing to its high stability, high energy laser systems, and high photocatalytic activities. For example, Ga dopant has been reported to increase the carrier concentration, electron mobility, and electronic conductivity of ZnO-based metal oxide, owing to highly degenerate Ga doping.[18, 19] Zhou et al. reported that {111} surface of $NaGa_2O_4$ photocatalyst exhibits remarkable enhancement of the

[a]Nano-Electro Mechanical Device Laboratory, School of Mechanical Engineering, Yonsei University, Seoul 120-749, South Korea
[b]School of Mathematics, University of East Anglia, Norwich, NR4 7TJ, United Kingdom
[c]Institute of Applied Physics and Materials Engineering, University of Macau, Avenida da Universidade, Macau, China.
*E-mail: bizhui@umac.mo (Kwun Nam Hui)
*E-mail: k.hui@uea.ac.uk (Kwan San Hui)
*E-mail: scj@yonsei.ac.kr (Seong Chan Jun)

View Article Online
DOI: 10.1039/C7TA05493A

photocatalytic water splitting for H_2 and O_2 evolution due to high mixed occupied Ga/Ni ratio compared to {100} facets.[15] However, $NiGa_2O_4$ spinel structure has seldom been explored in the field of energy storage. Until very recently, Zhang *et al*., pioneered a hydrothermal synthesis of Ga-doped NiO cathode material for supercapacitor applications.[20] The results revealed that Ga doping in NiO structure enabled a higher specific capacitance and exceptional cycling stability compared to NiO, signifying the importance of Ga doped Ni-based oxides for potential application in supercapacitors. However, to the best of author knowledge, the influence of Ga on the electrochemical performance of Ni-based spinel structure was not reported and fully understood. Therefore, in this study, we aim to understand and unravel the role of Ga on the electrochemical performance of a new class $NiGa_2O_4$ spinel structure as an advanced cathode electrode for supercapacitors. To the best of our knowledge, the role of Ga in improving the electrochemical performance of Ni–Ga spinel materials for supercapacitors has not been reported and is still unclear.

By contrast, despite the great progress of cathode materials, the electrochemical performance of anode materials should be fully considered to maximize the energy density and widen the operation voltage window of asymmetric supercapacitor (ASC) devices. Among these anode materials, hematite (Fe_2O_3) shows superior electrochemical performance in the negative potential owing to its high theoretical capacitance, low cost, and nontoxicity.[21] Significant efforts have been devoted to improving the electrochemical performance of Fe_2O_3 by the use of one-dimensional (1D) nanostructures, such as nanorods,[22] nanowires,[23] and nanotubes.[21] The high specific capacitance and enhanced cycling stability are attributed to the efficient transport pathway between the electrons and ions. Thus, Fe_2O_3, with a well-defined spindle structure, is anticipated to be a desirable material for anode electrodes.

In this study, we investigate for the first time the mechanism of Ga in a nickel gallate ($NiGa_2O_4$) spinel structure in enhancing the specific capacitance, rate capability, and cycling durability, reaching a specific capacitance of 1508 F g^{-1}, an increase of 95% with respect to the undoped NiO. We systematically investigate a series of $NiGa_2O_4$ nanosheets hydrothermally grown on Ni foam at different growth times (4, 8, 12, and 16 h). An advanced ASC device was constructed on the basis of the optimized hierarchical porous $NiGa_2O_4$ nanosheets at 12 h ($NiGa_2O_4$-12 h) as the positive electrode and spindle-like Fe_2O_3 as the negative electrode. The ASC device exhibits a high cell capacitance of 146 F g^{-1} at 1 A g^{-1}, a maximum energy density of 45.2 W h kg^{-1} at a power density of 1600 W kg^{-1}, and remarkable cycling stability with a retention of 94.3% specific capacitance after 10,000 cycles. Rietveld refinement provides solid evidence that the cubic lattice parameter *a* increases in $NiGa_2O_4$, such that the diffusion coefficient of the OH^- ion and the high rate capability of the material are significantly enhanced compared to NiO nanosheets. In addition, Ga substitution shortens the bond lengths of M-M and M-O (M represents Ni or Ga) as a result of the smaller size of Ga^{3+} compared to Ni^{2+}; this phenomenon decreases the volume of the MO_6 octahedron, thereby improving the structural stability and cycling stability. Moreover, the electrical conductivity measurements prove that the substitution of Ga^{3+} for Ni^{2+} improves the electronic conductivity during the electrochemical reaction; consequently, a high rate performance is obtained.

2. Experimental section

2.1. Material preparation

2.1.1. Synthesis of $NiGa_2O_4$ nanosheets. All chemicals were used as received without further purification. Prior to deposition, a piece of Ni foam (2 cm × 2 cm) was pretreated using 2 M HCl solution with ultrasonication for 15 min; these samples were then rinsed with acetone and deionized water to ensure a clean surface. Typically, 1 mmol of $Ni(NO_3)_2{\cdot}6H_2O$ and 2 mmol of $Ga(NO_3)_3{\cdot}xH_2O$ were dissolved in a mixed solvent of 80 mL deionized water. Next, 1.44 g urea and 0.44 g NH_4F were slowly added under continuous stirring. The pretreated Ni foam and the obtained homogeneous solution was then transferred to a Teflon-lined stainless-steel autoclave, which was sealed and maintained at 120 °C for different reaction times (4, 8, 12, and 16 h). After cooling down to room temperature, the Ni substrates with as-synthesized products were collected and rinsed with ultrasonication to remove the loosely attached products on the surface using deionized water and ethanol, followed by full drying at 80 °C. Thereafter, the Ni substrates with as-grown NiGa-precursors were calcined at 350 °C for 2 h with a temperature ramp rate of 2 °C min^{-1} in Ar atmosphere. The resulting $NiGa_2O_4$ with different hydrothermal times (4, 8, 12, and 16 h) were labeled as $NiGa_2O_4$-4 h, $NiGa_2O_4$-8 h, $NiGa_2O_4$-12 h, and $NiGa_2O_4$-16 h. The mass loadings of the aforementioned $NiGa_2O_4$ samples were determined to be 1.0, 1.2, 1.3, and 1.3 mg cm^{-2}, respectively. In the present synthesis scheme, the optimized $NiGa_2O_4$ nanosheets were grown on different conductive substrates (Cu foam and carbon fiber) via the same hydrothermal process; this method proves that the process is general for various energy storage and conversion applications. To illustrate the rationality of the present

View Article Online
DOI: 10.1039/C7TA05493A

work, we synthesized the NiO-12 h without the addition of Ga precursor using a similar process.

2.1.2. Synthesis of spindle-like Fe_2O_3. For the synthesis of spindle-like Fe_2O_3, 3 mM $FeCl_3 \cdot 6H_2O$ and 18 mM sodium nitrate ($NaNO_3$) were dissolved in 80 mL water. Thereafter, the obtained yellow solution was transferred into a 50 mL Teflon-lined stainless-steel autoclave using a facile hydrothermal process at 100 °C for 12 h; the solution was then dried at 60 °C for 12 h. The prepared precursors were converted into Fe_2O_3 by calcination at 450 °C in air for 2 h at a heating rate of 2 °C/min.

2.2. Material characterization

X-ray diffraction (XRD) patterns were collected using a Bruker D8 Advanced X-Ray Diffractometer with Ni-filtered Cu Kα radiation (λ = 1.5406 Å) at a voltage of 40 kV and a current of 200 mA. The composition and valence states of the prepared samples were analyzed by X-ray photoelectron spectroscopy (XPS, VG Scientific ESCALAB250), which was calibrated to the carbon peak C 1s at 284.6 eV. Field emission scanning electron microscopy (FESEM) images were acquired using a Hitachi S−4800. Transmission electron microscopy (TEM) images were obtained using a Talos F200 X. Scanning transmission electron microscopy with energy dispersive X-ray spectroscopy (STEM-EDS; Talos F200 X) mapping was used to identify the distributions of Ga, Ni, and O. The electrical conductivity of the sample pellets was measured by a four-probe machine (CMT-SR1000, AIT) at room temperature. The mass loss determination was performed in Ar atmospheres with a temperature ramp of 5 °C min^{-1} using a TA instruments apparatus (TGA Q50 V6.7 Build 203).

2.3. Electrochemical measurements

The electrochemical measurements were conducted in a three-electrode electrochemical system containing a 6 M KOH electrolyte at room temperature. The active material on Ni foam (1 cm × 1 cm) was selected as the working electrode. Pt foil and a saturated calomel electrode (SCE) were used as the counter and reference electrodes, respectively. Cyclic voltammetry (CV) and galvanostatic charge/discharge (GCD) were performed on an Ivium-n-Stat electrochemical workstation (Ivium, Netherlands). Electrochemical impedance spectrum measurements were conducted in a frequency range of 100 kHz to 0.1 Hz in the open circuit potential with an alternating current perturbation of 5 mV.

ASCs were packaged in a CR 2302 coin cell; in this cell, a $NiGa_2O_4$ nanosheet electrode, an Fe_2O_3 electrode, cellulose fabric, and a 6 M KOH solution were used as the positive electrode, negative electrode, separator, and electrolyte, respectively. The negative electrode was prepared as follows: the prepared Fe_2O_3, acetylene black, and polytetrafluoroethylene in the mass proportions of 85:10:5 were mixed together by adding a small amount of ethanol to produce a homogeneous mash. Then, the resulting slurry was coated onto a Ni foam current collector with mass loading of approximately 3 mg cm^{-2}. Finally, the fabricated electrode was pressed and dried at 80 °C overnight, and was then cut into a round film. The mass loading ratio of $NiGa_2O_4$ nanosheets to Fe_2O_3 was set to approximately 0.2 to obtain optimized electrochemical performance. The specific capacitance (C_{device}), energy density (E), and power density (P) were calculated from the GCD curves according to the following equations:[24, 25]

$$C_{device} = \frac{I \times \Delta t}{\Delta V \times M} \quad (1)$$

$$E = \frac{1}{2} C_{device} \Delta V^2 \quad (2)$$

$$P = \frac{E}{\Delta t} \quad (3)$$

where I is the discharge current (mA), Δt is the discharge time (s), M is the whole effective mass of the negative and positive electrodes (mg), and ΔV is the operating potential window of the device (V).

3. Results and discussion

The crystal structure of the NiGa-precursor was characterized by XRD analysis (**Figure S1a**), which is in good agreement with the NiGa-LDH reported in the literature.[26] The thermal behavior of the pristine NiGa-precursor was examined by TGA techniques. As shown in **Figure S1b**, the weight loss process can be divided into two steps. The first step can be ascribed to the desorption of inter-layered water and physically absorbed water, while the second step corresponds to dehydroxylation of the layers and decomposition of the carbonate anion.[27, 28] The phases of the $NiGa_2O_4$ and NiO were presented in **Figure S2**. The diffraction peaks centered at 2θ = 37.6°, 43.5°, and 63.2° can be assigned to the (111), (200), and (220) crystal planes of NiO phase (JCPDS no. 73-1519) with cubic structure and space group of *Fm-3m* (No. 225). For the $NiGa_2O_4$, the diffraction peaks at 30.6°, 36.1°, 58.1°, and 63.6° are clearly identified, corresponding to the (220), (311), (511), and (150) planes of the spinel $NiGa_2O_4$ phase (JCPDS card no. 78-0546) with cubic structure and space group of *Fd-3m* (No. 227). The broad reflection peaks observed in the patterns indicate the small grain size of $NiGa_2O_4$. XPS measurements were

View Article Online
DOI: 10.1039/C7TA05493A

conducted to investigate the composition and surface electron state of the porous $NiGa_2O_4$ nanosheets. The XPS full survey spectrum of $NiGa_2O_4$ indicates the existence of Ni, Ga, and O (**Figure S3**). The Ni/Ga atomic ratio for the prepared sample determined by the XPS analysis is approximately 0.53, which deviates slightly from the ratio of the reactants. This result may be attributed to the higher permissible capability of Ni^{2+} ions to precipitate in solution compared with Ga^{3+} ions. Using a Gaussian fitting method, the Ni 2p emission spectrum (**Figure 1a**) can be fitted well with two prominent spin–orbit doublets, characteristic of Ni oxidation states containing Ni^{2+} and Ni^{3+}, and two shakeup satellites at binding energies of 861.3 and 879.6 eV.[29, 30] The binding energy peaks at 854.0 and 872.0 eV are ascribed to Ni^{2+}, while the binding energy peaks at 855.9 and 873.9 eV correspond to Ni^{3+}.[30] The Ga 2p spectrum (**Figure 1b**) is fitted well with Ga 2p3/2 and Ga 2p1/2 peaks at 1118.1 and 1144.9 eV, respectively.[31] The energy separation between the two main peaks is approximately 26.8 eV, which is in accordance with the reference value of 26.84 eV.[32] Moreover, two peaks located at 19.1 and 21.3 eV are observed from the complex Ga 3d curve (**Figure 1c**).[31] The O 1s spectrum (**Figure 1d**) is fitted by three peaks, marked by O1, O2, and O3. The O1 peak at 530.0 eV is indexed to typical metal–oxygen bonds; the O2 contribution at 531.1 eV is attributed to the defect sites with low oxygen coordination, contaminants, and surface species; the O3 peak located at 532.5 eV is indexed to the multiplicity of physisorbed/chemisorbed water at or near the surface.[33]

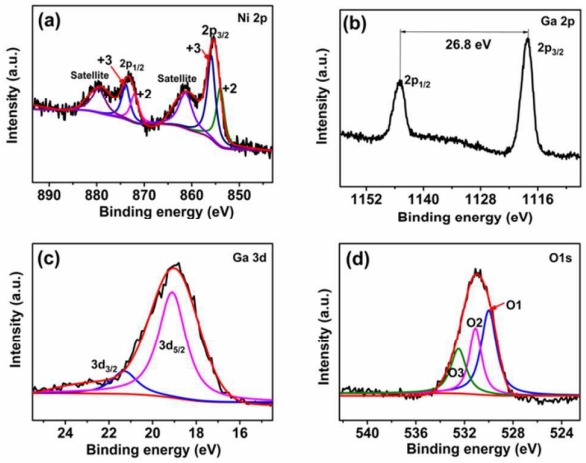

Figure 1. XPS survey scan of (a) Ni 2p spectrum, (b) Ga 2p spectrum, (c) Ga 3d spectrum, and (d) O 1s regions.

The evolutionary stages of the as-prepared $NiGa_2O_4$ with different hydrothermal reaction times (4, 8, 12, and 16 h) were explored. After being hydrothermally processed for 4 h, the interconnected nanosheet arrays with a transparent feature are found densely packed and uniformly grown on the skeleton of the NF substrate (**Figures 2a and S4**). When the reaction time is extended to 8 h, the nanosheets evidently become thick (**Figures 2b and S5**). When the reaction time is increased to 12 h (**Figures 2c and S6**), well-aligned structures with the large nominal width of these nanosheets are developed. The SEM image in **Figure 2c** shows that the interlaced nanosheet subunits are approximately 700 nm in length, 20 nm in thickness, and vertically aligned on the substrate, thereby forming a wall-like structure with possible good mechanical strength. EDS mapping analysis shows the existence of O, Ni, and Ga through the $NiGa_2O_4$-12 h nanosheets (**Figure S7**). With the on-going reaction, a trace of chips agglomerated at the surface of the corresponding products for 16 h is observed (**Figures 2d and S8**); this phenomenon may lead to the degradation of the electrochemical performance. Accordingly, we focus our investigation on the products with the hydrothermal reaction time of 12 h. As determined by the adsorption–desorption isotherm (**Figure S9**), the hierarchical porous $NiGa_2O_4$-12 h possesses a Brunauer–Emmett–Teller (BET) specific surface area of approximately 158 $m^2\ g^{-1}$, which is higher than those of $NiGa_2O_4$-4 h (57 $m^2\ g^{-1}$), $NiGa_2O_4$-8 h (96 $m^2\ g^{-1}$), and $NiGa_2O_4$-16 h (127 $m^2\ g^{-1}$). The pore size distribution curves of $NiGa_2O_4$ samples reveal the mesoporous characteristics having the average pore size ranges from 4.5 to 5.3 nm.

The high BET specific surface area and mesoporous structure are beneficial to enrich the electroactive sites and shorten diffusion paths for electrolyte ions; accordingly, the electrochemical performance is enhanced. Hierarchical $NiGa_2O_4$ nanosheet arrays supported on different types of conductive substrates (flexible carbon fiber and Cu foam) are presented (**Figure S10**) to further investigate the typical synthesis process for potential applications. The existence of a Cu foam supporter was verified by EDS mapping, as shown in **Figure S11**.

View Article Online
DOI: 10.1039/C7TA05493A

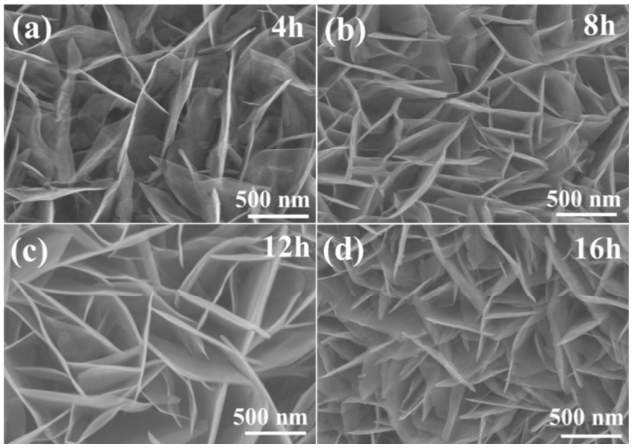

Figure 2. SEM images of the $NiGa_2O_4$ samples for different reaction times. (a) 4 h, (b) 8 h, (c) 12 h, and (d) 16 h.

TEM clearly reveals a smooth nanosheet morphology (**Figure 3a**). Figure 3a shows a single typical nanoplate of $NiGa_2O_4$. The hexagonal shape is a first indication that the nanosheet is single crystalline. **Figure 3b** reveals numerous pores with an average diameter of ~3.5 nm, homogeneously distributed on the surface. The (220) crystal planes with an interlayer spacing of 0.29 nm were observed in the high-resolution TEM (HRTEM) image (**Figure 3c**). The spacing measured from the HRTEM is consistent with our XRD results (**Figure S2**). Furthermore, families of {220} planes with interfacial angles of 60° are observed. This indicates that the exposed in-plane crystal plane is the {111} facet. The corresponding selected area electron diffraction (SAED) pattern in **Figure 3d**, further confirms the monocrystal nature of the $NiGa_2O_4$ nanosheets.

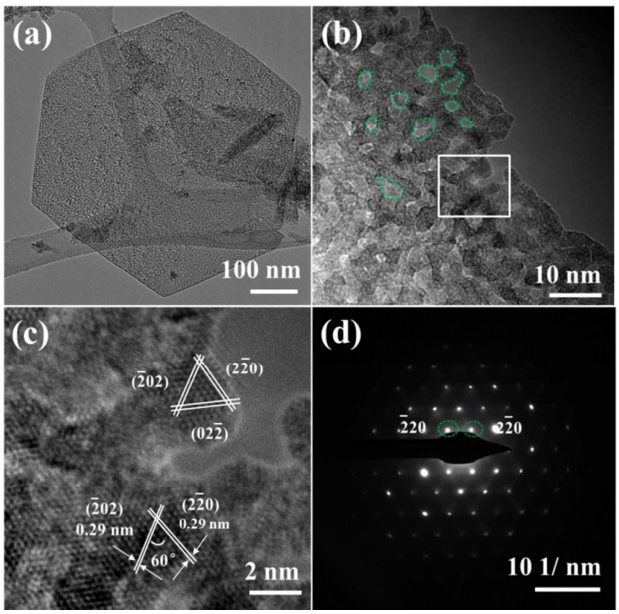

Figure 3. (a–b) TEM images, (c) HRTEM image of the selected area (white square) in (b), and (d) the corresponding SAED pattern of $NiGa_2O_4$-12 h.

Figure 4a shows the CV of pristine NiO-12 h and $NiGa_2O_4$ with different hydrothermal times (4, 8, 12, and 16 h) in 6 M KOH electrolyte at a scan rate of 30 mV s^{-1}. Visibly, a pair of well-defined redox peaks with anodic peaks at approximately 0.51 V vs. SCE and cathodic peaks around 0.31 V vs. SCE is observed for the as-prepared samples; these peaks originate mainly from the Faradaic redox reactions related to Ni-O/Ni-O-OH associated with OH^- anions in the electrolyte.[34] Notably, the pure NF substrate exhibits a negligible current compared with the as-fabricated samples (**Figure S12**); this finding shows that the capacitance contribution ratio from the NF (about 2.1% for $NiGa_2O_4$-12 h electrode) can be ignored. The area under the CV curve for the $NiGa_2O_4$ electrodes increases with the hydrothermal time, and it reaches a maximum for the $NiGa_2O_4$-12 h sample. However, the capacitance significantly decreases with further elongation of the hydrothermal time; this phenomenon may be ascribed to an excess deposition that leads to suppressed electrochemical activity. The CV curves of the $NiGa_2O_4$-12 h electrode with wide sweep rates ranging from 2 to 50 mV s^{-1} were recorded in the potential window of 0−0.65 V vs. SCE in further exploring the current response of the $NiGa_2O_4$-12 h electrode (**Figure 4b**). The sweep rate gradually increases to 50 mV s^{-1}, and the shapes of the CV curves show essentially trifling changes with distinct current peaks; therefore, the electrode material has low resistance. The GCD measurements were performed at a current density of 1 A g^{-1} (**Figure 4c**). As expected, the $NiGa_2O_4$-12 h electrode shows longer discharge times and thus higher specific capacitance than

View Article Online
DOI: 10.1039/C7TA05493A

the other electrodes. The obvious plateaus in the GCD curves imply the existence of a Faradaic behavior, which is consistent with the aforementioned CV results. GCD curves of the $NiGa_2O_4$-12 h (**Figure S13**) at various current densities ranging from 1 A g^{-1} to 20 A g^{-1} were obtained. The feature of the high symmetrical GCD curves with a slight IR drop is manifested by the low internal resistance and excellent electrochemical reversibility of the $NiGa_2O_4$-12 h electrode.

The specific capacitances of the as-synthesized electrodes, dependent on the discharge curves can be evaluated, as shown in **Figure 4d**. The respective specific capacitances of the pristine NiO-12 h and $NiGa_2O_4$ (4, 8, 12, and 16 h) electrodes are 722, 785, 1078, 1508, and 989 F g^{-1} at a current density of 1 A g^{-1}. The achieved specific capacitance of the $NiGa_2O_4$-12h electrode is also comparable with those of the reported Ni bimetallic-based electrodes, such as $NiCo_2O_4$ hollow spheres (1141 F g^{-1} at 1 A g^{-1}),[35] hollow $NiCo_2O_4$ nanoarrays (1055.3 F g^{-1} at 2.5 mA cm^{-2}),[36] copper–nickel oxide nanowires (1103.2 F g^{-1} at 10 mA cm^{-2}),[37] and nickel–manganese oxide nanoparticles/multiwall carbon nanotubes (803 F g^{-1} at 1 mA cm^{-2}).[38] When the current density is increased by up to 20 A g^{-1}, the retentions of specific capacitance values are 60.1%, 58.8%, 63.7%, and 56.4% for $NiGa_2O_4$ (4, 8, 12, and 16 h); these values are superior to those for pristine NiO-12 h (56.3%). The high rate capacities are also higher than the reported Ni-based electrodes, such as NiO nanoflowers (52.5% from 0.5 A g^{-1} to 5 A g^{-1}),[39] CNT/NiO nanosheets (50.2% from 1 A g^{-1} to 20 A g^{-1}),[40] and $NiCo_2O_4$@MnO_2 core–shell nanowires (50.2% from 2 mA cm^{-2} to 20 mA cm^{-2}).[41] The long-term cycling life at a high current density is a critical parameter for SCs to address the desired demands for commercial applications. **Figure 4e** shows that $NiGa_2O_4$-12 h delivers a high specific capacitance of 983 F g^{-1} after 10000 cycles, corresponding to a high capacitance retention of 102.4% at a high current density of 20 A g^{-1}; this value is obviously higher than that for NiO-12 h (44.9% capacitance retention). The prolonged cycling test is considered superior to those for Ni-based oxides/hydroxides/sulfides (**Table S1**). Electrochemical impedance spectroscopy curves of the samples were recorded in analyzing the electrical conductivity and dynamical characteristics of the electrodes.[42] The corresponding Nyquist spectra can be fitted with an equivalent circuit (**inset of Figure 4f**). The partial semicircle represents the interfacial charge transfer resistance (R_{ct}). As shown in **Figure 4f**, the R_{ct} values of the NiO-12 h and $NiGa_2O_4$ with different hydrothermal times (4, 8, 12, and 16 h) are 7.9, 10.4, 5.9, 5.5, and 6.3 Ω, respectively. Compared with the other electrodes, the low R_{ct} of $NiGa_2O_4$-12 h electrode tends to achieve a high charge transfer efficiency.[42] As observed in **Figure S14**, the R_{ct} values of NiO-12 h and $NiGa_2O_4$-12 h slightly increase after the cycling test, which indicates that the $NiGa_2O_4$-12 h sample retains desirable interfacial charge transfer resistances and good cycling stability compared to NiO-12 h sample.

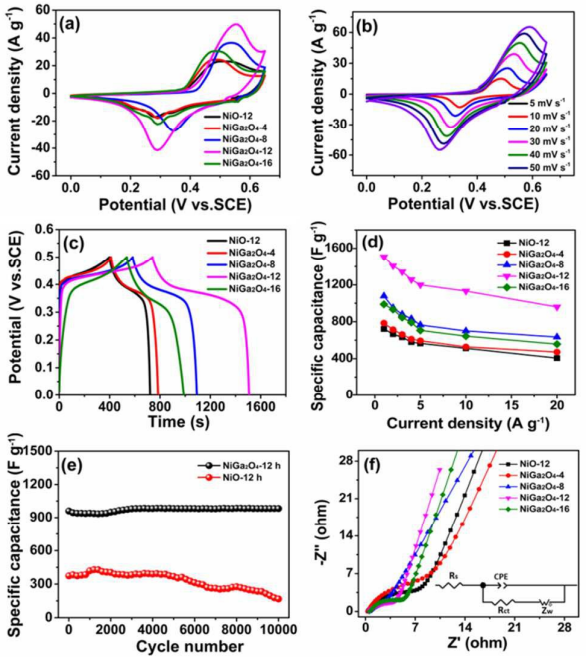

Figure 4. (a) CV curves of the NiO-12 h and $NiGa_2O_4$ (4, 8, 12, and 16 h). (b) CV curves of $NiGa_2O_4$-12 h at various scan rates from 5 mV s^{-1} to 50 mV s^{-1}; (c) GCD curves of the NiO-12 h and $NiGa_2O_4$ (4, 8, 12, and 16 h). (d) Specific capacitance dependent on current densities of electrodes; (e) cycling performance of the NiO-12 h and $NiGa_2O_4$-12 h at a current density of 20 A g^{-1}; and (f) Nyquist plots of these electrodes fitted with the corresponding equivalent circuit.

The exceptional supercapacitive performance can be attributed to the following facts: The ultrathin feature of nanosheets can shorten the OH^- ion diffusion distance and electron transportation path, thereby resulting in the high utilization of electroactive species; the void space between the nanosheets can effectively facilitate the penetration of electrolyte ions and accommodate the volume variation during continuous charge–discharge cycling; mechanically stable self-assembly without the addition of binders ensures favorable kinetics in electron/ion transportation.

SEM and TEM images were obtained after cycling to investigate the origin of the long-term stability of the $NiGa_2O_4$-12 h electrode. After the cycling test, the electrode still maintains good structural integrity. However, numerous petal-like layers form uniformly on the surface of the $NiGa_2O_4$ nanosheets (**Figures S15a–b**). The mechanical robustness feature is particularly beneficial for highly

View Article Online
DOI: 10.1039/C7TA05493A

exposed surface areas in efficiently increasing the utilization efficiency of active materials. A typical TEM image (**Figure S15c**) shows that the nanosheet surface is enclosed by folded layers. A magnified TEM image, shown in **Figure S15d**, displays the nanosheets comprising small nanoparticles and featuring numerous nanopores; these features allow the electrolyte ions to access and transport along the inner surface of the active materials efficiently. These results support the potential of $NiGa_2O_4$ nanosheets as electrodes for SCs with superior cycling performance.

We attempt to explore the role of Ga in improving the high rate capability and cycling performance of the newly explored $NiGa_2O_4$ spinel structure for SCs. Rietveld refinement using XRD data was analyzed. **Figure 5a** shows the Rietveld refinement results of the as-synthesized samples hydrothermally grown for 12 h ($NiGa_2O_4$-12 and NiO-12). The refined crystal structure of $NiGa_2O_4$ is shown in **Figure 5b**. The spinel $NiGa_2O_4$ adopts the structure with Ni^{2+} and Ga^{3+} cations occupying tetrahedral and octahedral sites. The lattice parameter values are calculated from the refinements and are found to be a = 4.1921(15) Å and 8.2977(81) Å for NiO and $NiGa_2O_4$, respectively (**Table S2**). Our Rietveld refinements show that the lattice parameter a is increased in $NiGa_2O_4$ compared with that in NiO; this finding indicates that the diffusion coefficient of the OH^- ions is enhanced, as well as the high rate capability of the material. Gao *et al*. applied density functional theory to investigate the binding energy of Li-rich Mn-based cathode materials; they concluded that a short bond length usually means a high binding energy, indicating the high stability of the crystal structure.[43] Our results show that the length of the Ga-Ga bonds in $NiGa_2O_4$ is significantly shorter than that of the Ni-Ni bonds in NiO, as a result of the smaller ionic size of Ga^{3+} (0.61 Å, coordination number: 4; 0.76 Å, coordination number: 6) compared to Ni^{2+} (0.83 Å, coordination number: 6); this finding indicates that $NiGa_2O_4$ has a higher structural and cycling stability of the crystal structure compared with the compound NiO. Moreover, the aliovalent substitution of Ga^{3+} for Ni^{2+} improves the electronic conductivity during electrochemical reactions, such that a high rate performance is obtained. The measured electrical conductivity of $NiGa_2O_4$ is 2.44 × 10^{-3} S m^{-1} compared to that of NiO (2.62 × 10^{-4} S m^{-1}), which verifies the contribution to the enhanced electrical conductivity by the aliovalent substitution of Ga^{3+} for Ni^{2+}. In addition, the spinel $NiGa_2O_4$ adopts the structure (*Fd-3m* space group) with Ni^{2+} and Ga^{3+} cations located in the center of O_4 tetrahedrons (Ga^{3+}) and O_6 octahedra (Ni^{2+} and Ga^{3+}), respectively.[44] Such edge-sharing octahedra established a three-dimensional network of tunnels that accounts for the efficient ion diffusion.[45]

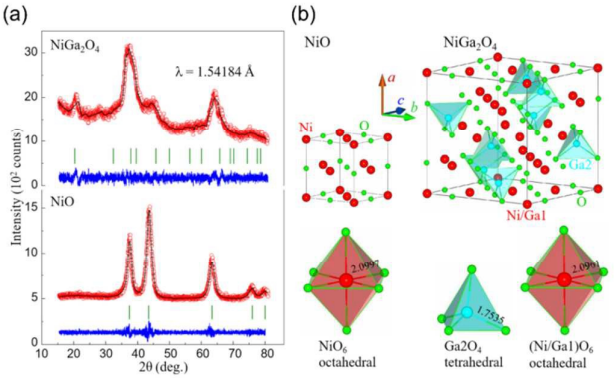

Figure 5. (a) Rietveld refinement patterns of XRD data for the NiO and $NiGa_2O_4$. (b) Crystal structures (with one unit cell shown as solid lines) and their building blocks of NiO (*Fm-3m*) and $NiGa_2O_4$ (*Fd-3m*). The building blocks are NiO_6 octahedral for NiO, and $Ga2O_4$ tetrahedral and $(Ni/Ga1)O_6$ octahedral for $NiGa_2O_4$. The corresponding shortest bond lengths of Ni-O (in NiO) and Ni(Ga1)-O and Ga2-O are marked in units of Å.

The XRD pattern of the as-synthesized Fe_2O_3 was obtained (**Figure S16a**). All the diffraction peaks can be indexed to the rhombohedral-type Fe_2O_3 phase (JCPDS Card no. 1-1053).[46] **Figure S16b** shows that Fe_2O_3 is composed of a large number of highly monodispersed spindle-like subunits. The subunits with smooth surfaces have a length of approximately 120 nm. Notably, numerous mesopores are uniformly distributed throughout the entire surface of the subunits; this phenomenon may be attributed mainly to the re-crystallization process and gas release during the calcination process.[47] TEM observations (**Figure S16c**) show that the spindle-like subunits comprise numerous large void spaces with sizes in the range of 20–30 nm; this finding is consistent with the SEM result. **Figure S16d** shows the lattice fringe with an interplanar spacing of 0.17 nm, which can be indexed to the (116) plane of the Fe_2O_3 phase. EDX spectroscopy data confirm the existence of Fe and O in the subunits (**Figure S17**). The CV curves of the Fe_2O_3 electrode at various scan rates ranging from 5 to 100 mV s^{-1} in the potential window of −0.9–0 V vs. SCE (**Figure S18a**). The similar rectangular shape of the CV curves is manifested by the Faradaic behavior of Fe_2O_3; this characteristic may arise from a reversible Fe^{3+}/Fe^{2+} coupling. The peak current increases with an insignificant change in the CV shape, although the scan rate increases to 100 mV s^{-1}; thus, the good electrochemical reversibility and high rate capability of the material is revealed. GCD measurements were conducted at various current densities ranging from 1 to 30 A g^{-1} (**Figure S18b**). The specific capacitance corresponds to 171.5 F g^{-1} at a current density of 1 A g^{-1}, and it remains at 86.7 F g^{-1} at a high

View Article Online
DOI: 10.1039/C7TA05493A

current density of 30 A g^{-1} (**Figure S18c**). In particular, the stable specific capacitance of 103 F g^{-1} can be retained for Fe_2O_3 after 5,000 cycles at 10 A g^{-1} with a capacitance retention of nearly 86% (**Figure S18d**); this performance indicates a good electrochemical stability. The outstanding rate capability and electrochemical stability can be attributed to the 1D spindle structure, which is conducive to fast ion diffusion and provides a short transport distance. To confirm the excellent performance of the spindle-like Fe_2O_3 electrode, the CV curves of the ASC device (**Figure 6b**) were collected at different scan rates ranging from 5 to 50 mV s^{-1}; these curves exhibit a sloped shape, indicating the contribution of Faradic capacitance from the ASC device.[48] A slight distortion is observed for the CV curves conducted at high scan rates, suggesting a good rate capability. GCD curves at different current densities with the potential window of 1.6 V are shown in **Figure 6c**. The nonlinear charge–discharge profiles demonstrate the Faradic behavior of the electrode.[49] The specific capacitance as a function of the discharge current density is plotted in **Figure 6d**. The capacitances based on the total mass can be calculated as 127, 115, 101, 94, 75, and 67 F g^{-1} at the current densities of 2, 3, 4, 5, 8, and 10 A g^{-1}, respectively. The leakage current and self-discharge characteristics of supercapacitor device are two parameters essential to evaluating its practical performance. As shown in **Figure S19**, the leakage current of the constructed $NiGa_2O_4$//Fe_2O_3 ASC device rapidly decreases at first and then stabilizes at 39 μA after maintaining a constant voltage for 2 h. The output voltage reaches around 0.94 V after 24 h, which demonstrates good energy storage performance and high stability of the ASC device. The Ragone plot of the $NiGa_2O_4$//Fe_2O_3 ASC device derived from the discharge curves is shown in **Figure 6e**. An energy density of 45.2 Wh kg^{-1} can be achieved at a power density of 1,600 W kg^{-1}, and it remains at 23.8 Wh kg^{-1}, even at a high power density of 8,000 W kg^{-1}; these values are advantageous over those for previously reported devices.[50-54] **Figure 6f** shows the cycling performance of the ASC device measured at a current density of 10 A g^{-1} up to 10,000 cycles. Notably, the ASC device delivers an outstanding capacitance retention of 94.3% after the cycling test. Such cycling performance is highly competitive with those of previous reports (**Table S3**). This can be attributed to a large number of electrochemical active sites of the $NiGa_2O_4$ nanosheets, as well as the facile access and fast diffusion path provided by the spindle-like Fe_2O_3.

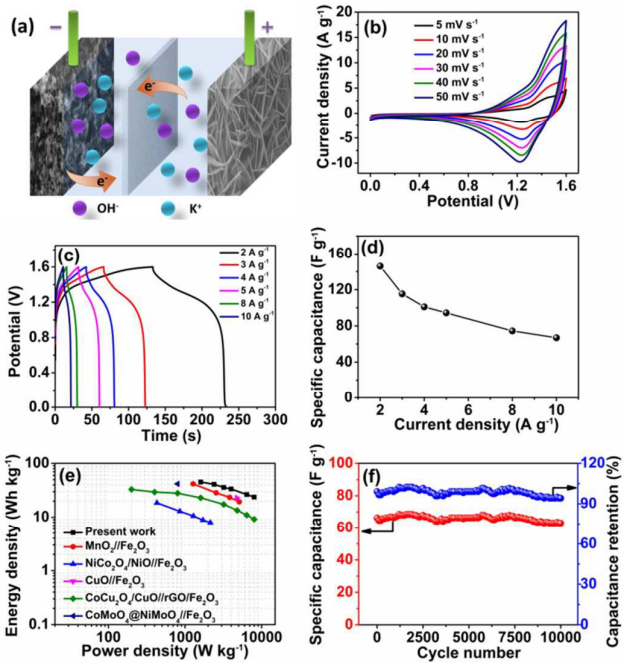

Figure 6. (a) Schematic of the $NiGa_2O_4$-12 h//Fe_2O_3 ASC device. (b) CV curves at different scan rates from 5 mV s^{-1} to 50 mV s^{-1}; (c) GCD curves in the potential range from 0 V to 1.6 V; (d) specific capacitance versus current density; (e) Ragone plots; and (f) cyclic stability at 10 A g^{-1}.

4. Conclusions

In summary, we have successfully developed new spinel-type porous $NiGa_2O_4$ nanosheets by a facile method. The Rietveld refinement reveals that the increased structure stability and improved ion diffusion kinetics of the $NiGa_2O_4$ electrodes arise from the aliovalent substitution of Ga^{3+} for Ni^{2+} in the spinel structure. Given the large exposed active surface of its hierarchical nanoscale porous structure and chemically stable interface, the $NiGa_2O_4$ electrode exhibits a high specific capacitance of 1508 F g^{-1} at a current density of 1 A g^{-1}, a good rate capability (63.7% retention at 20 A g^{-1}), and an excellent cycling stability of 102.4% retention after 10,000 cycles. More remarkably, the $NiGa_2O_4$//Fe_2O_3 ASC device delivers a high energy density of 45.2 Wh kg^{-1} at a power density of 1600 W kg^{-1}. Furthermore, the device exhibits exceptional cycling stability, with approximately 94.3% cell capacitance retention after 10000 cycles. All these results indicate that the aliovalent substitution between different cations and efficient structural design presented here could pave the way for other electrochemical systems.

Acknowledgements

View Article Online
DOI: 10.1039/C7TA05493A

This work was supported by the Science and Technology Development Fund from Macau SAR (FDCT-098/2015/A3), the Start-up Research Grant (SRG2015-00057-FST) from Research & Development Office at University of Macau, UEA funding, and the Korean Government (MSIP) (No. 2015R1A5A1037668) through the National Research Foundation of Korea (NRF) funded by the Ministry of Education, Science, and Technology (MEST).

Notes and references

1 K. Wang, X. Zhang, C. Li, X. Sun, Q. Meng, Y. Ma and Z. Wei, Adv. Mater., 2015, 27, 7451-7457.

2 Y. Li, Z. Li and P. K. Shen, Adv. Mater., 2013, 25, 2474-2480.

3 L. Xuan, L. Chen, Q. Yang, W. Chen, X. Hou, Y. Jiang, Q. Zhang and Y. Yuan, J. Mater. Chem. A, 2015, 3, 17525-17533.

4 H. Liang, C. Xia, Q. Jiang, A. N. Gandi, U. Schwingenschlögl and H. N. Alshareef, Nano Energy, 2017, 35, 331-340.

5 G. Zhang and X. W. D. Lou, Adv. Mater., 2013, 25, 976-979.

6 S. Dai, B. Zhao, C. Qu, D. Chen, D. Dang, B. Song, J. Fu, C. Hu, C.-P. Wong and M. Liu, Nano Energy, 2017, 33, 522-531.

7 Z.-D. Huang, K. Zhang, T.-T. Zhang, X. Li, R.-Q. Liu, X.-M. Feng, Y. Li, X.-J. Lin, Y.-B. He and X.-S. Yang, J. Mater. Chem. A, 2015, 3, 20886-20891.

8 R. R. Salunkhe, J. Lin, V. Malgras, S. X. Dou, J. H. Kim and Y. Yamauchi, Nano Energy, 2015, 11, 211-218.

9 G. D. Yuan, W. J. Zhang, J. S. Jie, X. Fan, J. X. Tang, I. Shafiq, Z. Z. Ye, C. S. Lee and S. T. Lee, Adv Mater, 2008, 20, 168-+.

10 Y. K. Tseng, C. J. Huang, H. M. Cheng, I. N. Lin, K. S. Liu and I. C. Chen, Adv. Funct. Mater., 2003, 13, 811-814.

11 L. Y. Zhang and H. Gong, Electrochim. Acta, 2016, 191, 270-274.

12 P. Yang, Y. Ding, Z. Lin, Z. Chen, Y. Li, P. Qiang, M. Ebrahimi, W. Mai, C. P. Wong and Z. L. Wang, Nano Lett., 2014, 14, 731-736.

13 Y. Jiao, Y. Liu, B. Yin, S. Zhang, F. Qu and X. Wu, Nano Energy, 2014, 10, 90-98.

14 U. Cvelbar, Z. Chen, M. K. Sunkara and M. Mozetič, Small, 2008, 4, 1610-1614.

15 J. Cheng, Y. Lu, K. Qiu, H. Yan, J. Xu, L. Han, X. Liu, J. Luo, J.-K. Kim and Y. Luo, Sci Rep-Uk, 2015, 5, 12099.

16 L. Qian, L. Gu, L. Yang, H. Yuan and D. Xiao, Nanoscale, 2013, 5, 7388-7396.

17 M. Han, K. Jiang, J. Zhang, W. Yu, Y. Li, Z. Hu and J. Chu, J. Mater. Chem., 2012, 22, 18463-18470.

18 Y. Yuan, W. Du and X. Qian, J. Mater. Chem., 2012, 22, 653-659.

19 X.-F. Lu, D.-J. Wu, R.-Z. Li, Q. Li, S.-H. Ye, Y.-X. Tong and G.-R. Li, J. Mater. Chem. A, 2014, 2, 4706-4713.

20 S. Ci, Z. Wen, Y. Qian, S. Mao, S. Cui and J. Chen, Sci Rep-Uk, 2015, 5, 11919.

21 L. Shen, L. Yu, X. Y. Yu, X. Zhang and X. W. D. Lou, Angew. Chem. Int. Ed., 2015, 54, 1868-1872.

22 C. Guan, X. Liu, W. Ren, X. Li, C. Cheng and J. Wang, Adv. Energy Mater., 2017, DOI: 10.1002/aenm.201602391.

23 R. Li, Z. Lin, X. Ba, Y. Li, R. Ding and J. Liu, Nanoscale Horizons, 2016, 1, 150-155.

24 Y.-H. Li, Q.-Y. Li, H.-Q. Wang, Y.-G. Huang, X.-H. Zhang, Q. Wu, H.-Q. Gao and J.-H. Yang, Appl Energy, 2015, 153, 78-86.

25 S.-I. Kim, J.-S. Lee, H.-J. Ahn, H.-K. Song and J.-H. Jang, Acs Appl Mater Inter, 2013, 5, 1596-1603.

26 H. Yi, H. Wang, Y. Jing, T. Peng and X. Wang, J. Power Sources, 2015, 285, 281-290.

27 L. Yu, G. Zhang, C. Yuan and X. W. D. Lou, Chem. Commun., 2013, 49, 137-139.

28 G. Xiong, P. He, D. Wang, Q. Zhang, T. Chen and T. S. Fisher, Adv. Funct. Mater., 2016, 26, 5460–5470

29 Y. R. Gao, X. F. Wang, J. Ma, Z. X. Wang and L. Q. Chen, Chem Mater, 2015, 27, 3456-3461.

30 R. S. Kalubarme, H. S. Jadhav, D. T. Ngo, G.-E. Park, J. G. Fisher, Y.-I. Choi, W.-H. Ryu and C.-J. Park, Sci Rep-Uk, 2015, 5, 13266.

31 L. Li, S. Peng, Y. Cheah, P. Teh, J. Wang, G. Wee, Y. Ko, C. Wong and M. Srinivasan, Chem. Eur. J., 2013, 19, 5892-5898.

32 Y. Ye, J. Chen, Q. Ding, D. Lin, R. Dong, L. Yang and J. Liu, Nanoscale, 2013, 5, 5887-5895.

33 L. Zhang, B. Wu, N. Li, D. Mu, C. Zhang and F. Wu, J. Power Sources, 2013, 240, 644-652.

34 S. Jiang, Y. Sun, H. Dai, P. Ni, W. Lu, Y. Wang, Z. Li and Z. Li, Electrochim. Acta, 2016, 191, 364-374.

35 D. Du, R. Lan, W. Xu, R. Beanland, H. Wang and S. Tao, J. Mater. Chem. A, 2016, 4, 17749-17756.

View Article Online
DOI: 10.1039/C7TA05493A

36 G. S. Gund, D. P. Dubal, N. R. Chodankar, J. Y. Cho, P. Gomez-Romero, C. Park and C. D. Lokhande, Sci Rep-Uk, 2015, 5, 12454.

37 A. Shanmugavani and R. K. Selvan, Electrochimica Acta, 2016, 189, 283-294.

38 A. V. Shinde, N. R. Chodankar, V. C. Lokhande, A. C. Lokhande, T. Ji, J. H. Kim and C. D. Lokhande, RSC Adv., 2016, 6, 58839-58843.

39 Y. Wang, C. Shen, L. Niu, R. Li, H. Guo, Y. Shi, C. Li, X. Liu and Y. Gong, J. Mater. Chem. A, 2016, 4, 9977-9985.

40 J. Wang, L. Zhang, X. Liu, X. Zhang, Y. Tian, X. Liu, J. Zhao and Y. Li, Sci Rep-Uk, 2017, 7, 41088.

1. K. Wang, X. Zhang, C. Li, X. Sun, Q. Meng, Y. Ma and Z. Wei, *Advanced Materials*, 2015, 27, 7451-7457.
2. Y. Li, Z. Li and P. K. Shen, *Advanced Materials*, 2013, 25, 2474-2480.
3. Z. Zhang, S. Liu, J. Xiao and S. Wang, *Journal of Materials Chemistry A*, 2016, 4, 9691-9699.
4. S. Liu, K. Hui and K. Hui, *ACS applied materials & interfaces*, 2016, 8, 3258-3267.
5. S. Liu, K. Hui, K. Hui, V. V. Jadhav, Q. X. Xia, J. M. Yun, Y. Cho, R. S. Mane and K. H. Kim, *Electrochimica Acta*, 2016, 188, 898-908.
6. G. Zhang and X. W. D. Lou, *Advanced materials*, 2013, 25, 976-979.
7. T. Wang, Q. Le, G. Zhang, S. Zhu, B. Guan, J. Zhang, S. Xing and Y. Zhang, *Electrochimica Acta*, 2016, 211, 627-635.
8. M. Kuang, Y. X. Zhang, T. T. Li, K. F. Li, S. M. Zhang, G. Li and W. Zhang, *Journal of Power Sources*, 2015, 283, 270-278.
9. Z.-Y. Yu, L.-F. Chen and S.-H. Yu, *Journal of Materials Chemistry A*, 2014, 2, 10889-10894.
10. B. Guan, Q. Y. Shan, H. Chen, D. Xue, K. Chen and Y. X. Zhang, *Electrochimica Acta*, 2016, 200, 239-246.
11. S. Liu, K. H. Kim, J. M. Yun, A. Kundu, K. V. Sankar, U. M. Patil, C. Ray and S. C. Jun, *Journal of Materials Chemistry A*, 2017, 5, 6292-6298.
12. S. Liu, K. V. Sankar, A. Kundu, M. Ma, J.-Y. Kwon and S. C. Jun, *ACS Applied Materials & Interfaces*, 2017, 9, 21829–21838.
13. Q. A. Acton, *Heavy Metals-Advances in Research and Application: 2012 Edition*, ScholarlyEditions, 2012.
14. X. J. Lv, S. X. Zhou, X. Huang, C. J. Wang and W. F. Fu, *Appl Catal B-Environ*, 2016, 182, 220-228.
15. S. X. Zhou, X. J. Lv, C. Zhang, X. Huang, L. Kang, Z. S. Lin, Y. Chen and W. F. Fu, *Chempluschem*, 2015, 80, 223-230.
16. H. Xue, Z. H. Li, Z. X. Ding, L. Wu, X. X. Wang and X. Z. Fu, *Cryst Growth Des*, 2008, 8, 4511-4516.
17. X.-J. Lv, S. Zhou, X. Huang, C. Wang and W.-F. Fu, *Applied Catalysis B: Environmental*, 2016, 182, 220-228.
18. G. D. Yuan, W. J. Zhang, J. S. Jie, X. Fan, J. X. Tang, I. Shafiq, Z. Z. Ye, C. S. Lee and S. T. Lee, *Adv Mater*, 2008, 20, 168-+.
19. Y. K. Tseng, C. J. Huang, H. M. Cheng, I. N. Lin, K. S. Liu and I. C. Chen, *Adv Funct Mater*, 2003, 13, 811-814.
20. L. Zhang and H. Gong, *Electrochimica Acta*, 2016, 191, 270-274.
21. P. Yang, Y. Ding, Z. Lin, Z. Chen, Y. Li, P. Qiang, M. Ebrahimi, W. Mai, C. P. Wong and Z. L. Wang, *Nano letters*, 2014, 14, 731-736.
22. Y. Jiao, Y. Liu, B. Yin, S. Zhang, F. Qu and X. Wu, *Nano Energy*, 2014, 10, 90-98.
23. U. Cvelbar, Z. Chen, M. K. Sunkara and M. Mozetič, *Small*, 2008, 4, 1610-1614.
24. S. Liu, S. C. Lee, U. M. Patil, C. Ray, K. V. Sankar, K. Zhang, A. Kundu, J. H. Park and S. C. Jun, *Journal of Materials Chemistry A*, 2017, 5, 4543-4549.
25. S. Liu, K. San Hui, K. N. Hui, J. M. Yun and K. H. Kim, *Journal of Materials Chemistry A*, 2016, 4, 8061-8071.
26. O. Altuntasoglu, U. Unal, S. Ida, M. Goto and Y. Matsumoto, *Journal of Solid State Chemistry*, 2008, 181, 3257-3263.
27. L. Xiong, W. D. Zhang, Q. S. Shi and A. P. Mai, *Polymers for Advanced Technologies*, 2015, 26, 495-501.
28. S. Mallakpour and M. Dinari, *RSC Advances*, 2015, 5, 28007-28013.
29. J. Cheng, Y. Lu, K. Qiu, H. Yan, J. Xu, L. Han, X. Liu, J. Luo, J.-K. Kim and Y. Luo, *Sci. Rep.*, 2015, 5, 12099.
30. L. Qian, L. Gu, L. Yang, H. Yuan and D. Xiao, *Nanoscale*, 2013, 5, 7388-7396.
31. M. Han, K. Jiang, J. Zhang, W. Yu, Y. Li, Z. Hu and J. Chu, *J. Mater. Chem.*, 2012, 22, 18463-18470.
32. Y. Yuan, W. Du and X. Qian, *J. Mater. Chem.*, 2012, 22, 653-659.
33. X.-F. Lu, D.-J. Wu, R.-Z. Li, Q. Li, S.-H. Ye, Y.-X. Tong and G.-R. Li, *J. Mater. Chem. A*, 2014, 2, 4706-4713.
34. S. Ci, Z. Wen, Y. Qian, S. Mao, S. Cui and J. Chen, *Sci. Rep.*, 2015, 5, 11919.
35. L. Shen, L. Yu, X. Y. Yu, X. Zhang and X. W. D. Lou, *Angewandte chemie International Edition*, 2015, 54, 1868-1872.
36. C. Guan, X. Liu, W. Ren, X. Li, C. Cheng and J. Wang, *Advanced Energy Materials*, 2017, DOI: 10.1002/aenm.201602391.
37. R. Li, Z. Lin, X. Ba, Y. Li, R. Ding and J. Liu, *Nanoscale Horizons*, 2016, 1, 150-155.
38. Y.-H. Li, Q.-Y. Li, H.-Q. Wang, Y.-G. Huang, X.-H. Zhang, Q. Wu, H.-Q. Gao and J.-H. Yang, *Applied Energy*, 2015, 153, 78-86.
39. S.-I. Kim, J.-S. Lee, H.-J. Ahn, H.-K. Song and J.-H. Jang, *ACS Appl. Mater. Inter.*, 2013, 5, 1596-1603.
40. H. Yi, H. Wang, Y. Jing, T. Peng and X. Wang, *J. Power Sources*, 2015, 285, 281-290.
41. L. Yu, G. Zhang, C. Yuan and X. W. D. Lou, *Chem. Commun.*, 2013, 49, 137-139.
42. G. Xiong, P. He, D. Wang, Q. Zhang, T. Chen and T. S. Fisher, *Adv Funct Mater*, 2016, 26, 5460–5470
43. Y. R. Gao, X. F. Wang, J. Ma, Z. X. Wang and L. Q. Chen, *Chem Mater*, 2015, 27, 3456-3461.
44. R. S. Kalubarme, H. S. Jadhav, D. T. Ngo, G.-E. Park, J. G. Fisher, Y.-I. Choi, W.-H. Ryu and C.-J. Park, *Sci. Rep.*, 2015, 5, 13266.

View Article Online
DOI: 10.1039/C7TA05493A

45. L. Li, S. Peng, Y. Cheah, P. Teh, J. Wang, G. Wee, Y. Ko, C. Wong and M. Srinivasan, *Chem. Eur. J.*, 2013, 19, 5892-5898.

46. Y. Ye, J. Chen, Q. Ding, D. Lin, R. Dong, L. Yang and J. Liu, *Nanoscale*, 2013, 5, 5887-5895.

47. L. Zhang, B. Wu, N. Li, D. Mu, C. Zhang and F. Wu, *J. Power Sources*, 2013, 240, 644-652.

48. S. Jiang, Y. Sun, H. Dai, P. Ni, W. Lu, Y. Wang, Z. Li and Z. Li, *Electrochim Acta*, 2016, 191, 364-374.

49. D. Du, R. Lan, W. Xu, R. Beanland, H. Wang and S. Tao, *J. Mater. Chem. A*, 2016, 4, 17749-17756.

50. G. S. Gund, D. P. Dubal, N. R. Chodankar, J. Y. Cho, P. Gomez-Romero, C. Park and C. D. Lokhande, *Scientific reports*, 2015, 5, 12454.

51. A. Shanmugavani and R. K. Selvan, *Electrochimica Acta*, 2016, 189, 283-294.

52. A. V. Shinde, N. R. Chodankar, V. C. Lokhande, A. C. Lokhande, T. Ji, J. H. Kim and C. D. Lokhande, *RSC Advances*, 2016, 6, 58839-58843.

53. Y. Wang, C. Shen, L. Niu, R. Li, H. Guo, Y. Shi, C. Li, X. Liu and Y. Gong, *Journal of Materials Chemistry A*, 2016, 4, 9977-9985.

54. J. Wang, L. Zhang, X. Liu, X. Zhang, Y. Tian, X. Liu, J. Zhao and Y. Li, *Scientific Reports*, 2017, 7, 41088.

View Article Online
DOI: 10.1039/C7TA05493A

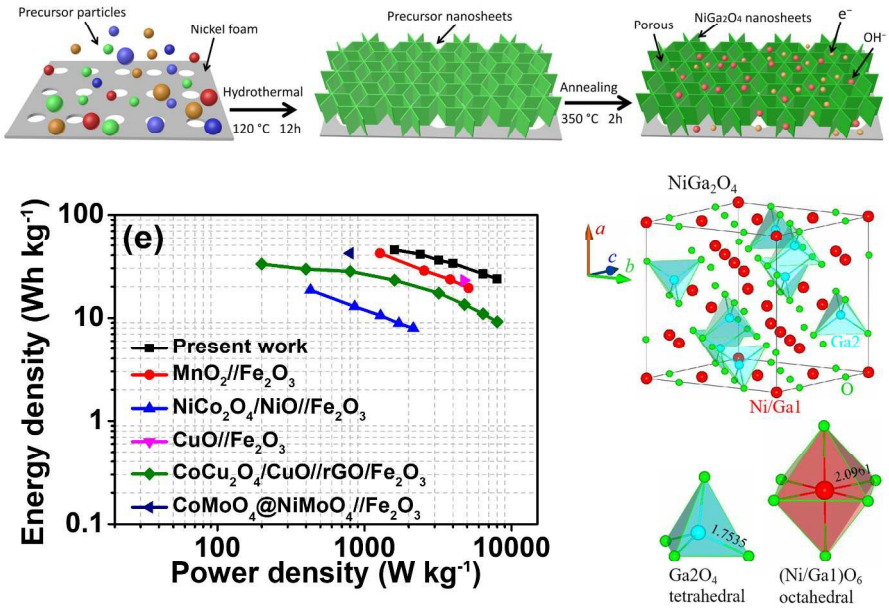

254x190mm (300 x 300 DPI)